Large-Amplitude Intermittent Swimming in Viscous and Inviscid Flows

Emre Akoz*
Lehigh University, Bethlehem, Pennsylvania 18015
Pan Han,† Geng Liu,‡ and Haibo Dong§
University of Virginia, Charlottesville, Virginia 22904
and
Keith W. Moored¶
Lehigh University, Bethlehem, Pennsylvania 18015

DOI: 10.2514/1.J056637

Recently, it was demonstrated in an inviscid flow that burst-and-coast or intermittent swimming can save energy when compared with continuous swimming and that the energy savings are maximized for large-amplitude pitching motions where flow separation is likely to occur. This paper examines the effects of flow separation on altering inviscid flow predictions. As such, viscous and inviscid flow simulations are presented of a hydrofoil pitching intermittently with large-amplitude motions. It is observed that leading-edge vortex formation and shedding in a viscous flow significantly alter the wake dynamics from the inviscid flow solutions where only trailing-edge shedding is modeled. Moreover, the inviscid flow solutions predict higher peak force production, lower cost of transport, and lower optimal duty cycles than the viscous flow solutions. Despite these differences, the trends in the force production and energetics seen in a viscous flow are well captured by the inviscid flow simulations. Importantly, both predict energy savings on the order of 10–30% for intermittent swimming, and the energy savings increase when the amplitude of motion is increased even when significant leading-edge separation occurs.

I. Introduction

AQUATIC animals use a variety of locomotion mechanisms and swimming gaits to propel themselves fast and efficiently through the oceans [1]. Some caudal fin swimmers, such as saithe [2], cod [3], and zebra danios [4], use an intermittent swimming gait known as burst-and-coast or burst-and-glide swimming. It was first hypothesized by Lighthill [5] that interspersing a coasting phase between steady swimming cycles can save energy for some fish to swim a given distance.

Classically, the observed energy savings have been attributed to the Bone–Lighthill boundary-layer thinning hypothesis [5]. This mechanism supposes that the skin friction drag coefficient is higher during the burst phase and lower during the coast phase of swimming due to the thinning of the boundary layer on a fish body when undulating [5–7]. By using this idea, Weihs [8] employed a simple dynamical model that assumes a drag increase during the burst phase of swimming to predict energy savings of over 50% when an intermittent gait is used instead of a continuous gait. This basic theory was verified by Wu et al. [9] with experiments conducted on intermittently swimming koi carp. They estimated energy savings of 45% at $Re = \mathcal{O}(10^4)$ by employing a vortex ring model to calculate the thrust of the fish. Furthermore, Chung [10] numerically examined the energetics of an intermittently swimming fish and reported energy savings of over 50% at $Re = \mathcal{O}(10^3)$.

Recently, Akoz and Moored [11] observed energy savings in an *inviscid* flow from a simple self-propelled hydrofoil pitching intermittently. For these computations, a high-Reynolds-number U^2 drag law was prescribed for the hydrofoil and, importantly, a fixed drag coefficient was used; that is, it did *not* follow the Bone–Lighthill hypothesis and rise during the burst phase. Yet, energy savings of more than 60% were discovered, indicating that there was also an inviscid mechanism behind the energy savings of intermittent swimming. It was further demonstrated that the energy savings are maximized for large-amplitude pitching motions in an inviscid flow. However, in a viscous flow it is likely that these large-amplitude motions will lead to flow separation, which can potentially dramatically alter the trends in energy savings observed in inviscid simulations.

Motivated by these observations, the current study aims to examine large-amplitude intermittent swimming in both viscous and inviscid flows to answer the following questions:

1) How are the wake dynamics of large-amplitude inviscid intermittent swimmers altered by flow separation?

2) Are the observed energy savings from inviscid simulations eliminated when there is separation?

3) If not, do energy savings increase with increasing amplitudes of motion in a viscous flow as well?

By answering these questions researchers will better understand when inviscid models can provide insights into the physics of intermittent swimming. Additionally, these answers will provide further guidance for understanding the impact of intermittent swimming on the energetics of fish.

II. Approach and Methods

An inviscid boundary element method (BEM) and a viscous immersed boundary method (IBM) are employed to differentiate the inviscid and viscous mechanisms contributing to the energetic benefit of intermittent swimming. Both methods are well-documented and validated in previous work and are consequently briefly introduced in the following sections.

A. Boundary Element Method

An unsteady potential flow method is employed to calculate the flow field around self-propelled hydrofoils. The flow is assumed to be

Presented as Paper 2017-3981 at the 47th AIAA Fluid Dynamics Conference, Denver, CO, 5–9 June 2017; received 17 August 2017; revision received 8 April 2019; accepted for publication 20 April 2019; published online 31 May 2019.

*Ph.D. Student, Department of Mechanical Engineering and Mechanics.
†Ph.D. Student, Department of Mechanical and Aerospace Engineering.
‡Postdoctoral Research Associate, Department of Mechanical and Aerospace Engineering.
§Associate Professor, Department of Mechanical and Aerospace Engineering.
¶Assistant Professor, Department of Mechanical Engineering and Mechanics.

irrotational (except on the boundary elements), incompressible, and inviscid, such that the velocity can be defined as $\boldsymbol{u} = \nabla\phi^*$, where ϕ^* is the perturbation potential in the inertial frame. The incompressible continuity equation is then reduced to Laplace's equation, $\nabla^2\phi^* = 0$, which governs the fluid flow. There is a general solution to Laplace's equation in the form of a boundary integral equation that is used to determine the potential field and the flowfield produced by a body and its wake. The general solution is applied subject to 1) a no flux boundary condition (i.e., no flux through the body boundaries), and 2) a far-field boundary condition that flow disturbances must decay far from the body. Following Katz and Plotkin [12], Quinn et al. [13], and Akoz and Moored [11], the general solution for the Laplace's equation is reduced to finding a distribution of doublets and sources on the hydrofoil surface and in the wake that satisfy the no-flux boundary condition on the body at each time step. Doublets and sources both implicitly satisfy the far-field boundary condition. We use the Dirichlet formulation to satisfy the no-flux condition on the foil body.

To solve this problem numerically, the hydrofoil is discretized into constant-strength source and doublet boundary elements and the wake is discretized into doublet elements. A no flux boundary condition is enforced at collocation points inside the body surface beneath each boundary element, leading to a linear system of equations. An explicit Kutta condition is applied at the trailing edge by setting the vorticity there to zero. At every time step, one wake panel is shed to satisfy Kelvin's condition. Shed panels advect with the local induced velocity field from the other wake and body elements. During this rollup process, the endpoints of the doublet elements, which are mathematically equivalent to point vortices, must be desingularized for the numerical stability of the solution. Following Krasny [14] the induced velocity on a wake element from other doublet elements is then calculated with a desingularized Biot–Savart law. During each time step, the unknown body doublet strengths can be determined and consequently the perturbation potential. The perturbation velocity on the body is then determined by a local differentiation of the perturbation potential. The pressure field acting on the body is calculated by using the perturbation velocity at the body surface in the unsteady Bernoulli equation. Finally, the forces acting on the pitching hydrofoil are calculated by an integration of the pressure forces over its boundary.

B. Immersed Boundary Method

The pitching foil is treated as an immersed moving boundary in the IBM-based computational fluid dynamics (CFD) solver. The numerical methodology employed in the current study is briefly introduced as the following. The 2D incompressible Navier–Stokes equations were discretized using a cell-centered, collocated arrangement of the primitive variables, and were solved using a finite-difference-based Cartesian grid IBM [15]. The immersed-boundary treatment is the same as that in [16]. The equations were integrated in time using the fractional step method, which consists of three steps. In the first substep of this method, a modified momentum equation is solved. A second-order Adams–Bashforth scheme is employed for the convective terms, whereas the diffusion terms are discretized using an implicit Crank–Nicolson scheme, which eliminates the viscous stability constraint. A second-order central difference scheme is employed in space discretization. This method was successfully applied in many simulations of flapping propulsion [17–20]. More details about this method can be found in Mittal et al. [15] and Dong et al. [16]. Validations about this solver can be found in our previous work of Li et al. [19] and Wan et al. [21].

C. Model Fidelity

Both modeling approaches are well-documented in previous work and have been extensively validated. However, they have different levels of model fidelity. The IBM used in this study is a high-fidelity method that models all of the relevant scales of fluid motion; that is, it is a direct numerical simulation of the Navier–Stokes equations, and as such it can be considered an exact solution. These simulations are computational costly due to the large number of grid points used during the simulations. The BEM is a medium-fidelity method where the physics are approximated by neglecting compressibility and viscosity. This leads to an inexact solution to the Navier–Stokes equations, but consequently is computationally cheap, leading to rapid simulations. It is expected that these modeling fidelity differences would lead to differences in the solutions especially in the wake dynamics; however, the global force production and energetics are expected to be well-captured by the BEM.

D. Problem Formulation

To investigate the role of flow separation in altering the wake dynamics, forces, and energetics of intermittent swimming recently found in inviscid flows, potential flow and DNS computations are employed with two-dimensional self-propelled hydrofoils. The inviscid BEM simulations and the viscous IBM simulations have identical geometries and kinematics described in the following sections.

1. *Geometry and Kinematics*

Following Akoz and Moored [11], a teardrop airfoil is chosen for the current study as shown in Fig. 1a, which has a semicircular leading edge that tapers along straight lines to its trailing edge. To understand the effect of hydrofoil geometry on leading-edge separation during intermittent swimming, three different maximum thickness profiles are considered. The maximum thicknesses ($t_{\max}$) of the hydrofoils are set to be 5, 10, and 15% of the chord length and the chord length of the airfoil is set to $c = 0.05$ m (see Fig. 1a). The hydrofoil undergoes intermittent pitching motions about its leading edge. The intermittent motion is a combination of a sinusoidal pitching motion during the burst period and it is followed by a fixed pitch angle of $\theta = 0$ during the coast period (see Fig. 1b). The total cycle period is simply the addition of the burst and coast periods. The ratio of the bursting period to the total cycle period is controlled by the duty cycle parameter:

$$\mathrm{DC} = \frac{\text{burst period}}{\text{total cycle period}} \tag{1}$$

The combined burst-and-coast kinematics of the hydrofoil are then defined as:

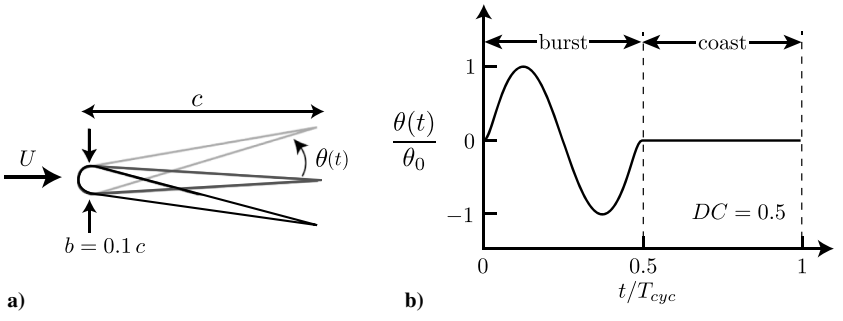

a) b)

Fig. 1 a) Geometric and kinematic parameters for the teardrop hydrofoil. b) Example pitch signal for an intermittent swimmer with DC = 0.5.

Table 1 Kinematic parameters used in the present study for both the inviscid BEM simulations and the viscous DNS

Continuous swimmers								
f (Hz)	0.25	0.5	0.75	1				
DC	1							
θ_0 (deg)	15	20						
t_{max}/c	0.05	0.1	0.15					
Intermittent swimmers								
f (Hz)	1							
DC	0.2	0.3	0.4	0.5	0.6	0.7	0.8	0.9
θ_0 (deg)	15	20						
t_{max}/c	0.05	0.1	0.15					

$$\theta(t) = \begin{cases} y_s(t)[\theta_0 \sin(2\pi f t)], & 0 \le t \le T_{\text{burst}} \\ 0, & T_{\text{burst}} \le t \le T_{\text{cycle}} \end{cases} \tag{2}$$

$$\text{where } y_s(t) = \begin{cases} -\tanh(kt)\tanh[k(t-1)], & \text{DC} < 1 \\ 1, & \text{DC} = 1 \end{cases} \tag{3}$$

where θ_0 is the pitch amplitude, f is the oscillation frequency, and t is the time. Equation (2) defines a reference signal where $0 \le t \le T_{\text{cycle}}$. The signal used in the simulations has N_{cyc} repetitions of this reference signal. Here, $T_{\text{burst}} = 1/f$ is the burst period and $T_{\text{cycle}} = T_{\text{burst}}/\text{DC}$ is the total cycle period. Also, two pitch amplitudes are used in the current study, namely, $\theta_0 = 15°$ and $\theta_0 = 20°$.

To obtain discretization-independent solutions as the time step size is reduced, the discontinuous angular rates and accelerations at the junction of the burst phase and coast phase must be smoothed. To do this, a hyperbolic tangent envelope function, $y_s(t)$, is multiplied with the sinusoidal burst signal and is defined in Eq. (3). This function modifies the slope of the sine wave at $t/T_{\text{burst}} = 0$ and $t/T_{\text{burst}} = 1$ to ensure a desingularized smooth junction with the coast phase where k controls the radius of curvature of the junction. Here a value of $k = 30$ is used throughout this study. Additionally, if DC $= 1$, then the signal (2) reverts to a continuous sinusoidal signal. In the current study the duty cycle ranges from DC $= 0.2$ to DC $= 1$ in 0.1 increments. A summary of the kinematic input parameters used in both the BEM simulations and the DNS is in Table 1.

Finally, the nondimensional mass of the swimmer is defined as the ratio of the mass of the swimmer, m, to the characteristic added mass of its propulsor:

$$m^* = \frac{m}{\rho S_p c} \tag{4}$$

Here ρ is the fluid density and S_p is the planform area of the propulsor. In the current study, the nondimensional mass is fixed to be $m^* = 1$ for both DNS and BEM simulations. This was chosen to minimize the time for the simulations to reach a cycle-averaged steady-state solution. It was also previously found that the self-propelled performance of a swimmer was nearly independent of the nondimensional mass as long as $m^* \ge 1$ [22].

2. Drag Model

In the inviscid simulations, a drag force D is imposed on the self-propelled pitching hydrofoil that acts to resist the motion of the swimmer. The magnitude of the drag force is determined from a drag law based on high-Reynolds-number swimming conditions (Munson et al. 1990) [23]:

$$D = 1/2\rho C_D S_w U^2 \tag{5}$$

where ρ is the density of the fluid, C_D is the drag coefficient, and U is the speed of the swimmer. The wetted surface area of the propulsor is S_w and is calculated by scaling the planform area by a constant, S_{wp}. This planform area–to–wetted surface area ratio in the current study is $S_{wp} = 2$.

To obtain the drag coefficient of the hydrofoils for the inviscid simulations, self-propelled swimming speeds of the hydrofoils from the DNS are used. Self-propelled swimming speeds of continuously swimming hydrofoils are recorded as a function of pitching frequency for both pitching amplitudes (Fig. 2a). The drag coefficients applied to the inviscid simulations are tuned such that the continuous motion self-propelled swimming speeds between the inviscid and viscous simulations match at the same pitching frequency. Following this methodology, drag coefficients are estimated over a range of self-propelled swimming speeds. Therefore, a power law relationship in the form of $C_d = c_1 U^{c_2} + c_3$ can represent the drag coefficients as a function of swimming speed (Fig. 2b). The drag coefficients of the inviscid simulations are estimated based on the power law relationship determined through the DNS data.

3. Output Performance

The free swimming condition is satisfied through a single-degree-of-freedom equation of motion that allows the streamwise translation of the hydrofoil. Following Borazjani and Sotiropoulos [24], the position and velocity of the swimmer at the $(n+1)$th time step is calculated by a trapezoidal rule and a forward differencing scheme, respectively:

$$x_{\text{LE}}^{n+1} = x_{\text{LE}}^{n} + \frac{1}{2}(U^{n+1} + U^{n})\Delta t \tag{6}$$

$$U^{n+1} = U^{n} + \frac{F_{x,\text{net}}^{n}}{m}\Delta t \tag{7}$$

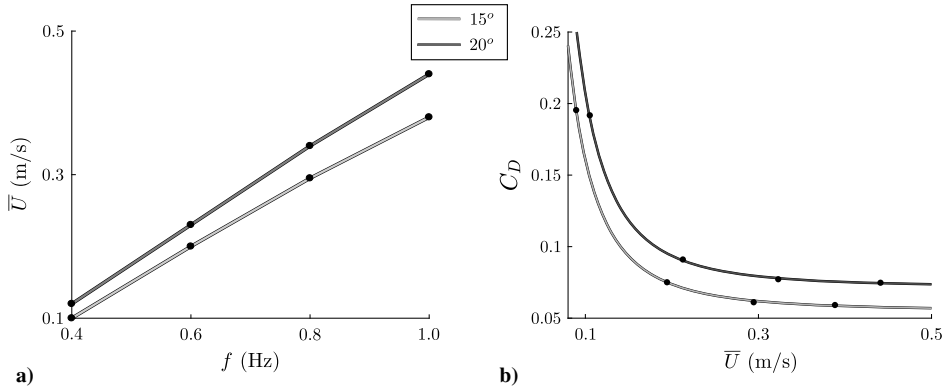

Fig. 2 a) Average self-propelled swimming speed of the hydrofoils as a function of pitching frequency for two different amplitudes of motion in DNS. b) Coefficient of drag as a function of average swimming speed. These data are obtained through matching the self-propelled swimming speed of the DNS results in the potential flow solver. The relationship in between $\bar{U}$ and C_d follows a power law relationship in the form of $C_d = c_1 U^{c_2} + c_3$. The coefficients are for 15°; $c_1 = 0.0001163$, $c_2 = -3.184$, and $c_3 = 0.08061$ and for 20°; $c_1 = 0.0002885$, $c_2 = -2.665$, and $c_3 = 0.05673$.

where Δt is the time step, $F^n_{x,\text{net}}$ is the net force acting on the hydrofoil in the streamwise direction at the nth time step, and x_{LE} is the position of the leading edge.

The thrust force is calculated as the streamwise force from the integration of the pressure forces only for the BEM simulations and from the integration of the pressure and shear forces for the DNS. The power input to the fluid is calculated as the negative inner product of the element force vector and element velocity vector of the hydrofoil, that is, $P = -\int_S F_{\text{ele}} \cdot u_{\text{ele}}\, \mathrm{d}\mathcal{S}$, where $\mathcal{S}$ is the body surface. The mean cruising velocity $\bar{U}$, mean thrust $\bar{T}$, and mean power $\bar{P}$ are time-averaged over a cycle once the swimmers have reached their cycle-averaged steady-state swimming conditions.

The cost of transport is defined as the amount of energy it takes to travel a unit distance per unit mass, and it is directly related to the range of a swimmer [22]. The thrust coefficient and cost of transport are defined as:

$$C_T \equiv \frac{\bar{T}}{\rho S_p f^2 A^2} \qquad \text{CoT} \equiv \frac{\bar{P}}{m\bar{U}} \tag{8}$$

Here the peak-to-peak amplitude of motion is A, which is related to the pitching amplitude as $A = 2c \sin\theta_0$. The ratio of the CoT of an intermittent swimmer to a continuous swimmer at the same mean speed is:

$$\hat{\text{CoT}} = \left.\frac{\text{CoT}^i}{\text{CoT}^c}\right|_{\bar{U}} \tag{9}$$

where CoT^i and CoT^c are the cost of transports for the intermittent and continuous swimmers, respectively. This cost of transport ratio directly determines the energetic savings or additional cost incurred by choosing intermittent swimming. For example, when $\hat{\text{CoT}} < 1$ it costs less energy to swim with an intermittent gait than a continuous gait. Conversely, when $\hat{\text{CoT}} > 1$ it costs more energy to swim with an intermittent gait than a continuous gait. Finally, if $\hat{\text{CoT}} = 1$ both intermittent and continuous swimming costs the same amount of energy.

III. Results

A. Wake Dynamics and Thrust Performance

Figures 3a–3d show the vorticity field of intermittently swimming hydrofoils at DC = 0.2 in an inviscid flow. Four distinct vortices are shed from the trailing edge of the hydrofoil during pitching. Vortices A and D are shed as the hydrofoil starts and stops pitching, respectively, whereas vortices B and C are shed as the hydrofoil changes direction. After the pitch oscillations cease and the hydrofoil enters the coast phase (Figs. 3c and 3d), no vortices are shed and the vortex groups A–D advect downstream. These inviscid wake dynamics are typical of intermittent swimming with one burst cycle and more details can be found in Akoz and Moored [11].

Figures 3e–3h show the vorticity field of the same intermittent swimmer operating in a viscous flow. The hydrofoil starts the motion in a relatively disturbed wake even at the lowest duty cycle studied, DC = 0.2. The absence of these vortices in the inviscid flow field and their presence in the viscous solution indicates that the vortex shedding does not stop in the coast phase of a viscous flow. Unlike the large stronger vortices observed in the inviscid flow field, the vortices are broken up into several smaller pieces. In Figs. 3e and 3f, a starting vortex A is similar to the inviscid simulations but vortex groups B and C consist of smaller separated vortices, which make the flow field significantly different from the inviscid solution. Stopping vortex D is observed to be stronger in the viscous flow. It is also broken up into several pieces and coalesces with the weak vortices shed during the coast phase. Also, the spacing between A, B, and C is larger in the viscous solution than in the inviscid solution. As a consequence, the positions of vortices A–D in Figs. 3g and 3h are significantly different from the inviscid solution. Additionally, unlike the inviscid wake, after the pitching motion ceases and the hydrofoil enters the coast

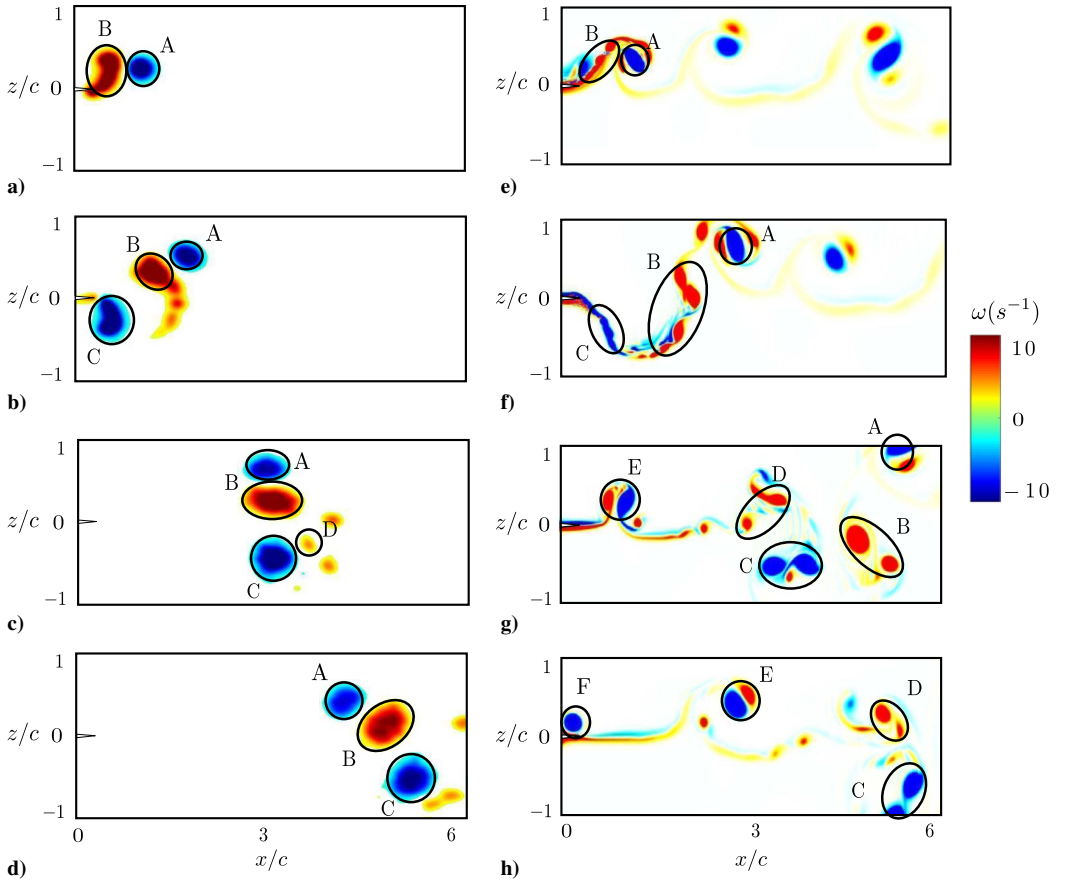

Fig. 3 The evolution of the vortex wake is shown for DC = 0.2 at nondimensional times of a,e) $t/T_{\text{cyc}} = 1/10$, b,f) $t/T_{\text{cyc}} = 2/10$, c,g) $t/T_{\text{cyc}} = 4/10$, and d,h) $t/T_{\text{cyc}} = 6/10$ in inviscid and viscous flows, respectively.

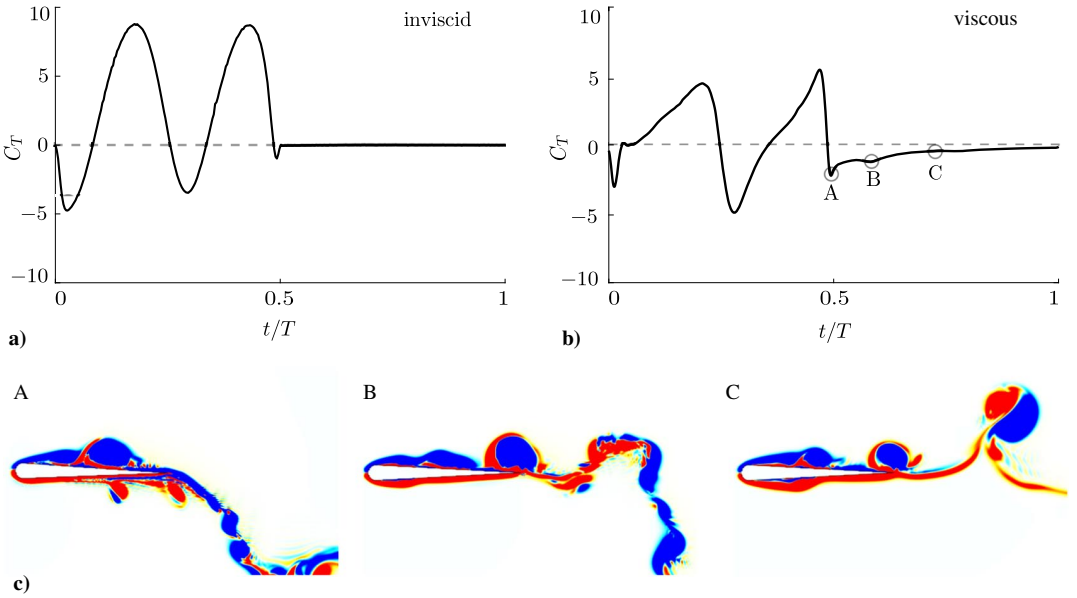

Fig. 4 Instantaneous thrust coefficients over a total period of an intermittent swimmer at DC = 0.5 in a) inviscid flow and b) a viscous flow at $Re \approx 5800$. c) Vorticity fields associated with points A, B, and C in (b).

phase, vortex pairs E and F are formed and shed into the wake. These vortex pairs can also be observed in Fig. 3e downstream of A and B, and their signatures can be observed in the instantaneous thrust described below, whereas they are completely absent from the inviscid solution.

Figures 4a and 4b show the instantaneous thrust of an intermittent swimmer over a cycle of motion for the inviscid and the viscous simulations, respectively. Swimmers show two peaks in the thrust that are associated with the shedding of the two strongest vortices B and C. Additionally, the formation of the starting and stopping vortices induces drag near $t/T = 0$ and $t/T = 0.5$. The thrust peaks and the induced drag trough from the starting vortex are all amplified in the inviscid case compared with the viscous solution. On the other hand, the induced drag from the stopping vortex is less pronounced in the inviscid flow than the viscous flow. Notably, the inviscid hydrofoil does not generate any thrust or experience any pressure drag (beyond the imposed drag from the drag law) during the coast period. In contrast, the hydrofoil in the viscous flow experiences pressure drag throughout the coast phase that decreases with time as shown in Fig. 4b by markers A, B, and C. This phenomenon can be linked to the formation and the shedding of leading-edge vortices during the coast phase as shown in Fig. 4c, where the vorticity field is shown at the respective times A, B, and C. Strong leading-edge vortices are formed right after the burst phase, which results in significant form drag at the beginning of the coast period. As the coast phase progresses, there is further formation of the leading-edge vortices; however, their size and intensity decay, and if the coast phase lasts long enough, both the vorticity field and the thrust curve recover back to a static hydrofoil state.

B. Energetics

1. *Amplitude Effect on Swimming Performance*

Figures 5a and 5b present the cost of transport as a function of the mean swimming speed for hydrofoils with pitch amplitudes of $\theta_0 = 15°$ and $\theta_0 = 20°$, respectively. The dashed lines represent the continuous swimmers, whereas the solid lines represent the intermittent swimmers. In general, as the frequency of motion of the continuous swimmers increases, their speed increases as does their CoT. Once $f = 1$ Hz and DC $= 1$ the intermittent and continuous swimmers' CoT curves are coincident. Then, as the duty cycle decreases (frequency fixed at $f = 1$ Hz) there is a decrease in the swimmers' speed and consequently a decrease in their CoT as well. Although the flow fields of viscous and inviscid swimmers are significantly different, both the DNS and BEM solutions show that there is a region where intermittent swimming has a lower cost of transport than continuous swimming at the same mean speed. In an inviscid flow, as velocity decreases (duty cycle decreases), the energy savings increase, which is measured as the difference between the continuous and intermittent swimmers' CoT curves at the same speed. The difference reaches its peak value at some DC, and further decreasing of the DC decreases the energy savings. The overall trend is similar for the viscous flow solutions except that the maximum benefit is observed for higher duty cycles. Furthermore, there is significant crossover of the curves at low DC, leading to an additional energetic cost for intermittent swimming above continuous swimming at the same mean speed.

Figures 5c and 5d present the normalized cost of transport as a function of DC and Re. The normalized cost of transport is similar for high duty cycles (DC > 0.5) in both viscous and inviscid flows, and an optimal duty cycle that maximizes the energy savings can be observed. For the lowest amplitude case, the maximum energy savings are 21% for the inviscid simulations and 9% for the viscous simulations (Fig. 5c). The higher amplitude case, on the other hand, shows a maximum of 29% and 18% energy savings for the inviscid and viscous swimmers, respectively (Fig. 5d). The maximum benefit occurs at DC $= 0.6$ in the DNS results and at DC $= 0.4$ in the BEM results. For DC < 0.4, continuous swimming is advantageous over intermittent swimming in the viscous simulations. In contrast, in the inviscid simulations intermittent swimming is shown to be beneficial regardless of the DC; however, the magnitude of the benefit decreases for DC < 0.4. It can also be observed that higher amplitudes of motion increase the energy savings in both viscous and inviscid simulations, even when there is significant leading-edge separation.

In previous studies [4,11,25,26], the effect of Re variation on intermittent swimming was examined. Here, the Re is connected to the inviscid simulations through the drag coefficient. When the duty cycle decreases, C_D increases and continuous swimming becomes energetically more favorable than intermittent swimming even in an inviscid flow [11]. This is further verified with the DNS results of the current study. A future study of higher Re DNS solutions would give a better idea of the energetic benefits of intermittent swimming because the Reynolds number of the simulations ($Re = \mathcal{O}(10^3)$) is on the lower end of the spectrum where fish start to swim intermittently in biology.

2. *Thickness Effect on Swimming Performance*

To understand the sensitivity of leading-edge separation on the hydrofoil thickness and in turn its effect on intermittent swimming performance, two other hydrofoil profiles are considered with a maximum hydrofoil thickness of $t_{\max}/c = 0.05$ and $t_{\max}/c = 0.15$,

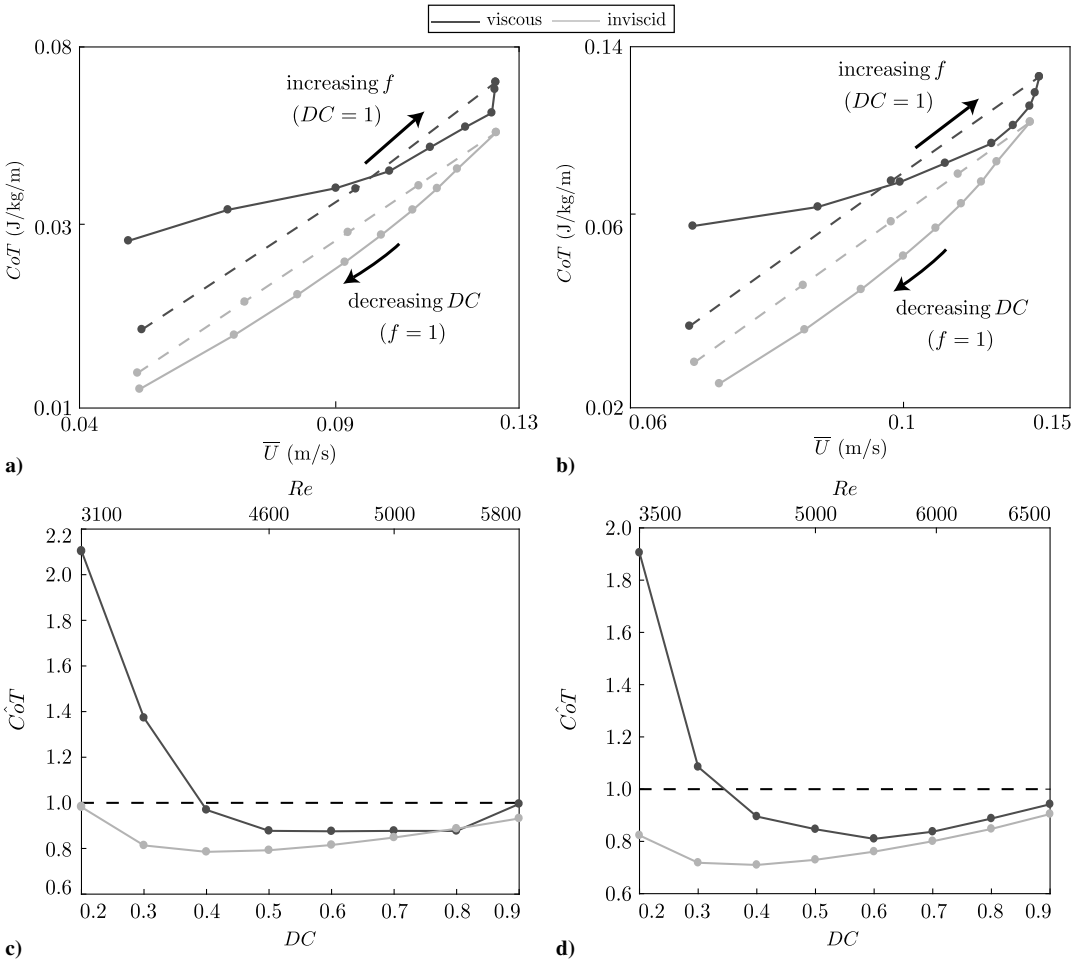

Fig. 5 Cost of transport as a function of velocity for DNS and BEM solutions and for maximum pitching amplitudes of a) $\theta_0 = 15°$ and b) $\theta_0 = 20°$. Dimensionless cost of transport as a function of DC in DNS and BEM solvers c) $\theta_0 = 15°$ and d) $\theta_0 = 20°$. The dashed lines represent the continuous swimmers, whereas the solid lines represent the intermittent swimmers.

where $t_{\max}/c$ is the hydrofoil thickness-to-chord ratio. Figure 6a shows the normalized cost of transport as a function of DC for $\theta_0 = 20°$ in a viscous flow. The overall trend of the curves are similar for all thicknesses. The energy savings increase as duty cycle decreases and reaches a maximum at DC $= 0.6$. Then, as duty cycle further decreases, continuous swimming becomes more beneficial for DC < 0.4. Furthermore, the energetic advantage of intermittent swimming decreases for increasing hydrofoil thickness. The maximum energy savings are 23% for the thinnest hydrofoil and 16% for the thickest hydrofoil.

Figure 6b shows the thrust coefficient over a pitching period at DC $= 0.5$ for all three thicknesses. The two peaks in thrust become higher and the troughs become lower as the hydrofoil thickness increases. Particularly, $t_{\max}/c = 0.05$ has a significantly compressed thrust curve over the pitching period compared with the other two profiles studied. Similarly, decreasing the thickness leads to a drag reduction in the coasting phase ($t/T > 0.5$).

The vorticity fields associated with the three different thickness hydrofoils at $t/T = 0.5$, $t/T = 0.58$, and $t/T = 0.72$ are shown in Fig. 7. As the profile becomes thinner, the leading-edge vortices become more elongated in shape, but do not show signs of weakening. However, the frontal area over which they act to produce form drag is greatly reduced with a decrease in the thickness. This in turn leads to the drag reduction during the coasting phase observed in

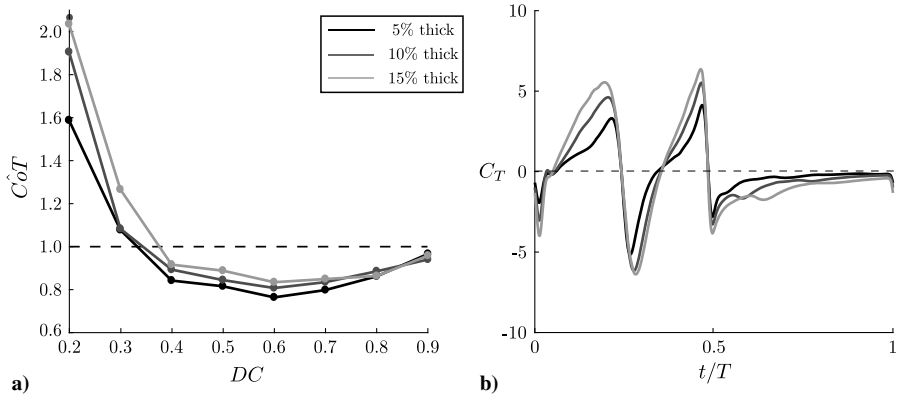

Fig. 6 a) Normalized cost of transport as a function of DC for $\theta_0 = 20°$. b) Thrust coefficients over a period of motion at DC $= 0.5$. Different colors represent different maximum hydrofoil thicknesses.

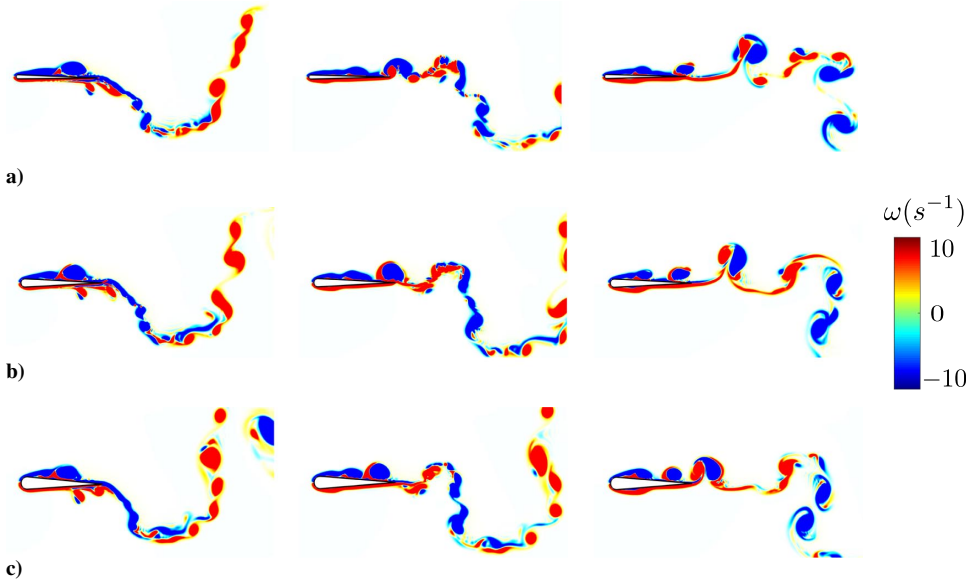

Fig. 7 Vorticity fields of hydrofoils with different maximum thicknesses at $t/T = 0.5$, $t/T = 0.58$, and $t/T = 0.72$. a) $t_{\max}/c = 0.05$, b) $t_{\max}/c = 0.1$, c) $t_{\max}/c = 0.15$.

Fig. 6b. Additionally, the reduced drag during the coasting phase is responsible for the increased energy savings during intermittent swimming as the profile thickness is reduced.

IV. Conclusions

The wake structures and the performance of self-propelled intermittently pitching hydrofoils are examined in viscous and inviscid flows. Although there are some similarities in the wakes between the simulations, there are significant differences that occur due to leading-edge vortex formation and shedding. In fact, leading-edge vortices are formed during the coast phase, resulting in additional form drag in the viscous simulations. Surprisingly, the hydrofoil thickness has little effect on the leading-edge vortex formation characteristics, yet thinner profiles experience lower form drag during the coast phase due to their smaller projected frontal area. This in turn leads to larger energy savings during intermittent swimming for the thinnest profiles. The energy savings reported as the normalized cost of transport are found to be in good agreement between the viscous and inviscid results for high duty cycles of DC > 0.5. For low duty cycles of DC ≤ 0.5 the results begin to deviate. In both simulations there is an optimal duty cycle to maximize the energy savings. In a viscous flow for $\theta_0 = 15°$ and $20°$ the maximum energy savings are 9 and 18%, respectively, whereas in an inviscid flow the energy savings are 21 and 29%, respectively. Moreover, both simulations show that the higher amplitude motions increase the maximum energy savings, even with significant leading-edge separation. Despite the differences in vortex shedding and the wake dynamics, the trends in the instantaneous forces and the energetics are similar between the simulations. This suggests that inviscid flow simulations can offer a rapid tool for investigating the trends in the performance of intermittent swimmers.

Acknowledgment

This work was funded by the Office of Naval Research under Program Director B. Brizzolara (MURI Grant No. N00014-14-1-0533).

References

[1] Sfakiotakis, M., Lane, D. M., and Davies, J. B. C., "Review of Fish Swimming Modes for Aquatic Locomotion," *IEEE Journal of Oceanic Engineering*, Vol. 24, No. 2, 1999, pp. 237–252. doi:10.1109/48.757275

[2] Videler, J. J., and Weihs, D., "Energetic Advantages of Burst-and-Coast Swimming of Fish at High Speeds," *Journal of Experimental Biology*, Vol. 97, No. 1, 1982, pp. 169–178.

[3] Videler, J. J., "Swimming Movements, Body Structure and Propulsion in Cod Gadus Morhua," *Symposium of the Zoological Society of London*, Vol. 48, 1981, pp. 1–27.

[4] Müller, U. K., Stamhuis, E. J., and Videler, J. J., "Hydrodynamics of Unsteady Fish Swimming and the Effects of Body Size: Comparing the Flow Fields of Fish Larvae and Adults," *The Journal of Experimental Biology*, Vol. 203, No. 2, 2000, pp. 193–206.

[5] Lighthill, M. J., "Large-Amplitude Elongated-Body Theory of Fish Locomotion," *Proceedings of the Royal Society B: Biological Sciences*, Vol. 179, No. 1055, Nov. 1971, pp. 125–138. doi:10.1098/rspb.1971.0085

[6] Ehrenstein, U., and Eloy, C., "Skin Friction on a Moving Wall and Its Implications for Swimming Animals," *Journal of Fluid Mechanics*, Vol. 718, 2013, pp. 321–346. doi:10.1017/jfm.2012.613

[7] Ehrenstein, U., Marquillie, M., and Eloy, C., "Skin Friction on a Flapping Plate in Uniform Flow," *Philosophical Transactions of the Royal Society A*, Vol. 372, No. 2020, 2014, Paper 20120345. doi:10.1098/rsta.2013.0345

[8] Weihs, D., "Energetic Advantages of Burst Swimming of Fish," *Journal of Theoretical Biology*, Vol. 48, No. 1, 1974, pp. 215–229. doi:10.1016/0022-5193(74)90192-1

[9] Wu, G., Yang, Y., and Zeng, L., "Kinematics, Hydrodynamics and Energetic Advantages of Burst-and-Coast Swimming of Koi Carps (Cyprinus Carpio Koi)," *Journal of Experimental Biology*, Vol. 210, No. 12, 2007, pp. 2181–2191. doi:10.1242/jeb.001842

[10] Chung, M.-H., "On Burst-and-Coast Swimming Performance in Fish-Like Locomotion," *Bioinspiration & Biomimetics*, Vol. 4, No. 3, 2009, Paper 036001. doi:10.1088/1748-3182/4/3/036001

[11] Akoz, E., and Moored, K. W., "Unsteady Propulsion by an Intermittent Swimming Gait," *Journal of Fluid Mechanics*, Vol. 834, No. 1, 2018, pp. 149–172. doi:10.1017/jfm.2017.731

[12] Katz, J., and Plotkin, A., *Low Speed Aerodynamics*, 13th ed., Vol. 13, Cambridge Univ. Press, Feb. 2001, pp. 331–342.

[13] Quinn, D. B., Moored, K. W., Dewey, P. A., and Smits, A. J., "Unsteady Propulsion Near a Solid Boundary," *Journal of Fluid Mechanics*, Vol. 742, March 2014, pp. 152–170. doi:10.1017/jfm.2013.659

[14] Krasny, R., "A Study of Singularity Formation in a Vortex Sheet by the Point-Vortex Approximation," *Journal of Fluid Mechanics*, Vol. 167, June 1986, pp. 65–93. doi:10.1017/S0022112086002732

[15] Mittal, R., Dong, H., Bozkurttas, M., and Najjar, F. M., "A Versatile Sharp Interface Immersed Boundary Method for Incompressible Flows with Complex Boundaries," *Journal of Computational Physics*,

Vol. 227, No. 10, 2008, pp. 4825–4852.
doi:10.1016/j.jcp.2008.01.028

[16] Dong, H., Mittal, R., and Najjar, F. M., "Wake Topology and Hydrodynamic Performance of Low-Aspect-Ratio Flapping Foils," *Journal of Fluid Mechanics*, Vol. 566, Nov. 2006, pp. 309–343.
doi:10.1017/S002211200600190X

[17] Liu, G., Ren, Y., Zhu, J., Bart-Smith, H., and Dong, H., "Thrust Producing Mechanisms in Ray-Inspired Underwater Vehicle Propulsion," *Theoretical and Applied Mechanics Letters*, Vol. 5, No. 1, 2015, pp. 54–57.
doi:10.1016/j.taml.2014.12.004

[18] Liu, G., Dong, H., and Li, C., "Vortex Dynamics and New Lift Enhancement Mechanism of Wing Body Interaction in Insect Forward Flight," *Journal of Fluid Mechanics*, Vol. 795, May 2016, pp. 634–651.
doi:10.1017/jfm.2016.175

[19] Li, C., Dong, H., and Liu, G., "Effects of a Dynamic Trailing-Edge Flap on the Aerodynamic Performance and Flow Structures in Hovering Flight," *Journal of Fluids and Structures*, Vol. 58, No. 10, 2015, pp. 49–65.
doi:10.1016/j.jfluidstructs.2015.08.001

[20] Li, C., and Dong, H., "Three-Dimensional Wake Topology and Propulsive Performance of Low-Aspect-Ratio Pitching-Rolling Plates," *Physics of Fluids*, Vol. 28, No. 7, 2016, Paper 071901.
doi:10.1063/1.4954505

[21] Wan, H., Dong, H., and Gai, K., "Computational Investigation of Cicada Aerodynamics in Forward Flight," *Journal of the Royal Society Interface*, Vol. 102, No. 12, 2015, Paper 20141116.

[22] Moored, K. W., and Quinn, D. B., "Inviscid Scaling Laws of a Self-Propelled Pitching Airfoil," *AIAA Journal*, Aug. 2018, pp. 1–15.
doi:10.2514/1.J056634

[23] Munson, B. R., Young, D. F., and Okiishi, T. H., *Fundamentals of Fluid Mechanics*, Wiley, 1990.

[24] Borazjani, I., and Sotiropoulos, F., "Numerical Investigation of the Hydrodynamics of Anguilliform Swimming in the Transitional and Inertial Flow Regimes," *Journal of Experimental Biology*, Vol. 212, No. 4, 2009, pp. 576–592.
doi:10.1242/jeb.025007

[25] Weihs, D., "Energetic Significance of Changes in Swimming Modes During Growth of Larval Anchovy Engraulis Mordax," *Fishery Bulletin*, Vol. 77, 1980, pp. 597–604.

[26] Noda, T., Fujioka, K., Fukuda, H., Mitamura, H., Ichikawa, K., and Arai, N., "The Influence of Body Size on the Intermittent Locomotion of a Pelagic Schooling Fish," *Proceedings of the Royal Society*, Vol. 283, No. 1832, 2016, Paper 20153019.

P. Givi
Associate Editor